Nanotechnology and Precision Engineering
纳米技术与精密工程

RESEARCH ARTICLE | JUNE 18 2024

# Studying mechanism of anisotropic crack generation on C-, R-, A-, and M-planes of sapphire during ultra-precision orthogonal cutting using a visualized slip/fracture activation model

Suk Bum Kwon; Sangkee Min



*Nanotechnol. Precis. Eng.* 7, 043006 (2024)
https://doi.org/10.1063/10.0026318

Nanotechnology and Precision Engineering ARTICLE pubs.aip.org/aip/npe

Editor's Pick

# Studying mechanism of anisotropic crack generation on C-, R-, A-, and M-planes of sapphire during ultra-precision orthogonal cutting using a visualized slip/fracture activation model

Cite as: Nano. Prec. Eng. 7, 043006 (2024); doi: 10.1063/10.0026318
Submitted: 15 December 2023 • Accepted: 11 May 2024 •
Published Online: 18 June 2024



Suk Bum Kwon and Sangkee Min[a)]

## AFFILIATIONS

Department of Mechanical Engineering, University of Wisconsin–Madison, 1513 University Avenue, Madison, Wisconsin 53706, USA

[a)]Author to whom correspondence should be addressed: sangkee.min@wisc.edu

## ABSTRACT

With the growing demand for the fabrication of microminiaturized components, a comprehensive understanding of material removal behavior during ultra-precision cutting has become increasingly significant. Single-crystal sapphire stands out as a promising material for microelectronic components, ultra-precision lenses, and semiconductor structures owing to its exceptional characteristics, such as high hardness, chemical stability, and optical properties. This paper focuses on understanding the mechanism responsible for generating anisotropic crack morphologies along various cutting orientations on four crystal planes (C-, R-, A-, and M-planes) of sapphire during ultra-precision orthogonal cutting. By employing a scanning electric microscope to examine the machined surfaces, the crack morphologies can be categorized into three distinct types on the basis of their distinctive features: layered, sculptured, and lateral. To understand the mechanism determining crack morphology, visualized parameters related to the plastic deformation and cleavage fracture parameters are utilized. These parameters provide insight into both the likelihood and direction of plastic deformation and fracture system activations. Analysis of the results shows that the formation of crack morphology is predominantly influenced by the directionality of crystallographic fracture system activation and by the interplay between fracture and plastic deformation system activations.



**KEYWORDS**
**Anisotropic behavior, Crack morphology, Slip/fracture activation model, Single-crystal sapphire, Ultra-precision machining**



## I. INTRODUCTION

Single-crystal sapphire has great potential for wide use in a variety of industrial fields, owing to its superior mechanical, chemical, and optical properties. However, it is challenging to machine sapphire, since cracks can easily propagate on the machined surface owing to its high hardness and brittleness.[1,2] Ultra-precision cutting is one of the methods that have been adopted to solve this challenging issue, since it facilitates material removal in a ductile manner without cracks forming on the machined surface under specific machining parameters.[3] With a depth of cut below a specific nanometer range, the material removal behavior of brittle ceramics can exhibit ductile characteristics because of the ductile-to-brittle transition. However, to use sapphire on a nanoscale, it is important to establish a proper machining strategy for its machining without crack initiation.

The results of indentation tests at the nanoscale have shown that the material response of single-crystal sapphire is predominantly dependent on crystal orientation when an external force is applied. Nowak and Sakai[4] explained the mechanism of plastic deformation on the four major crystal planes of single-crystal sapphire in terms of slip/twinning activations on crystallographic

structures during the indentation tests. They used the concept of the Schmid factor to discuss how the external force is involved in activating the slip/twinning mechanisms of the material. Wang *et al.*[5] reported on the nanoscale characteristics of crack morphologies on single-crystal sapphire during indentation tests. They demonstrated that various crack morphologies were generated, depending on the crystal plane orientations. The results of these studies related to indentation tests have provided important inspiration for understanding the material removal behavior in single-crystal sapphire during ultra-precision cutting.

Extensive research has been performed to uncover the mechanisms underlying material removal behavior in single-crystal sapphire during ultra-precision cutting, focusing on the crystallographic orientations of the sapphire. The relationships between machining characteristics such as force, activation of slip/fracture systems, and ductile-to-brittle transition have been studied. Mizumoto *et al.*[6] conducted a study of the removal behavior of the C-plane of sapphire during ultra-precision cutting. They developed a slip/fracture activation model to quantify the probability of plastic and fracture deformations. Through an analysis of parameters derived from this model, they were able to provide explanations for anisotropic ductile-to-brittle transitions. Kwon and Min[7] investigated the characteristics of force generation during ultra-precision cutting on various crystal planes of sapphire, including the C-, R-, A-, and M-planes. They showed that the direction of the force generated during machining in the ductile mode has a significant relationship with the degree of slip/twinning activation. Yoon *et al.*[8] predicted the applied stress at the ductile-to-brittle transition by calculating the stress intensity factor on each crystal plane during ultra-precision cutting.

The molecular dynamics (MD) simulation method has also been employed to study the material removal behavior of single-crystal sapphire during nano-scratching tests or ultra-precision cutting. It offers the advantage of providing an opportunity to directly observe the inherent removal behavior of the material in real time, which is impossible through experimental methods. Kim *et al.*[9] used MD simulation to investigate the mechanism of plastic deformation occurring on the C-, R-, A-, and M-planes of sapphire during indentation and scratching tests. Lin *et al.*[10] conducted an MD simulation that replicated a spherical indenter scratching test along various cutting orientations on the C-plane of sapphire. They demonstrated the influence of slip activation on specific prismatic planes on crack morphology and stress distribution.

The study of crack formation is of great significance, since an understanding of the underlying mechanisms is essential for comprehending the material removal behavior. There have been a number of studies of the mechanisms of crack formation in ultra-precision orthogonal cutting of cubic crystalline materials such as $CaF_2$ and yttrium-stabilized zirconia (YSZ).[11–14] A comprehensive and intuitive explanation of the crack-forming mechanism has been obtained by employing the concept of fracture activations occurring normal to the crystal planes. However, when it comes to sapphire, which features a more intricate hexagonal crystallographic system, there have been no comprehensive explorations of a crack formation mechanism that encompasses all the major crystal planes (C-, R-, A-, and M-planes) of sapphire in the context of ultra-precision orthogonal cutting.

In our previous study, anisotropic ductile-to-brittle transition and crack morphologies on the R-plane of sapphire along various cutting orientations in ultra-precision machining were investigated on the basis of a modified slip/fracture activation model. The different values of the critical depth of cut along various cutting orientations were explained in terms of plastic deformation parameters, while the mechanism of formation of different crack morphologies was explained by the intersection of multiple cleavage fracture activations on the machined surface. It was also pointed out that if slip/twinning systems are multiply activated simultaneously, this may cause complicated interactions such as entanglement, which accelerate crack propagation.[15]

In the present study, a novel comprehensive analysis is conducted. First, a visualized slip/fracture activation model is applied to all the crystal planes of sapphire: the C-, R-, A-, and M-planes. The mechanism of crack generation at ductile-to-brittle transition is studied by evaluating the correlations of visualized *F*-parameters with crack morphologies. Second, for a better understanding of the crack-generation mechanism, the interactions between *P*- and *F*-parameters are considered and the mechanisms of formation of a crack morphology on the C-, R-, A-, and M-planes are explained.

## II. THEORETICAL APPROACH

### A. Modified slip/fracture activation model

The slip/fracture activation model calculates the likelihood of slip and fracture system activations based on the direction of the resultant force, thereby accounting for the anisotropy of the crystal. For a mathematical representation of the parameters involved, an orthogonal coordinate system is established. As shown in Fig. 1, the negative $x$ axis is in the $[11\bar{2}0]$ direction for the C- and R-planes and the [0001] direction for the A- and M-planes, the positive $y$ axis is rotated 90° from the $x$ axis in a counterclockwise direction, and

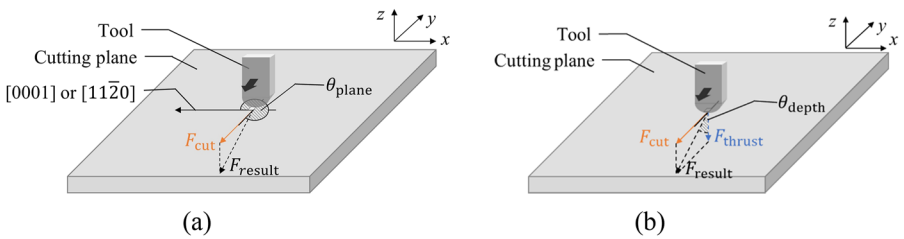


**FIG. 1.** Schematic representation of force directions in ultra-precision orthogonal cutting: (a) plane angle $\theta_{plane}$; (b) depth angle $\theta_{depth}$.

the direction of the positive $z$ axis is the opposite of the in-depth direction. On the basis of this coordinate system, the direction of the resultant force is determined by the cutting orientation on the plane, $\theta_{plane}$, and the cutting orientation in depth, $\theta_{depth}$, as shown in Fig. 1.

$\theta_{plane}$ is the clockwise angle between the pre-specified direction ([11$\bar{2}$0] for the C- and R-planes, [0001] for the A- and M-plane) and the cutting force $F_{cut}$ is the component of the resultant force projected onto the cutting plane. The thrust force $F_{thrust}$ is the component of the resultant force along the normal direction of the cutting plane. $\theta_{depth}$ can be expressed in terms of the cutting force and thrust force as $\theta_{depth} = \arctan(F_{cut}/F_{thrust})$. $\theta_{plane}$ is determined as a machining input, and $\theta_{depth}$ is calculated by measuring the cutting force and thrust force during machining.

The plastic deformation and cleavage fracture parameters for ultra-precision orthogonal cutting were suggested by Mizumoto *et al.*[6] and modified as follows to take account of the resultant force direction:[15]

$$P_i = \frac{\cos(\theta_{NP_i})\cos(\theta_{SP_i})}{\tau_i^{crit}/min_i\tau_i^{crit}}, \tag{1}$$

$$F_i = \frac{\cos^2(\theta_{NF_j})}{K_j^{IC}/\min_j K_j^{IC}}, \tag{2}$$

where $P_i$ is the plastic deformation parameter of the $i$-th slip system, $\theta_{NP_i}$ is the angle between the resultant force vector $(f_x, f_y, f_z)$ and the plane normal vector $(N_{ix}^{slip}, N_{iy}^{slip}, N_{iz}^{slip})$ of the $i$-th slip system, $\theta_{SP_i}$ is the angle between the resultant force vector and the shear direction vector $(S_{ix}^{slip}, S_{iy}^{slip}, S_{iz}^{slip})$ of the $i$-th slip system, and $\tau_i^{crit}$ is the critical resolved shear stress for the $i$-th slip system (with units of MPa). Here, the plane normal and shear direction vectors are unit vectors. $F_j$ is the cleavage fracture parameter of the $j$-th fracture system, $\theta_{NF_j}$ is the angle between the resultant force vector and the plane normal vector $(N_{jx}^{frac}, N_{jy}^{frac}, N_{jz}^{frac})$ of the $j$-th fracture system, and $K_j^{IC}$ is the mode I critical stress intensity factor for the $j$-th fracture system (with units of MPa m$^{0.5}$). Again, $(N_{jx}^{frac}, N_{jy}^{frac}, N_{jz}^{frac})$ is a unit vector. Therefore, $\cos(\theta_{NP_i})\cos(\theta_{SP_i})$ and $\cos^2(\theta_{NF_j})$ can be expressed as follows:

$$m_i = \cos(\theta_{NP_i})\cos(\theta_{SP_i}) = \cos\left(\frac{f_x N_{ix}^{slip} + f_y N_{iy}^{slip} + f_z N_{iz}^{slip}}{\sqrt{f_x^2 + f_y^2 + f_z^2}}\right)$$

$$\times \cos\left(\frac{f_x S_{ix}^{slip} + f_y S_{iy}^{slip} + f_z S_{iz}^{slip}}{\sqrt{f_x^2 + f_y^2 + f_z^2}}\right), \tag{3}$$

$$c_j = \cos^2(\theta_{NF_j}) = \cos^2\left(\frac{f_x N_{jx}^{frac} + f_y N_{jy}^{frac} + f_z N_{jz}^{frac}}{\sqrt{f_x^2 + f_y^2 + f_z^2}}\right), \tag{4}$$

where $m_i$ is the Schmid factor for the $i$-th slip system, indicating the contribution of the force direction to the activation of the slip system, and $c_j$ is the cleavage factor for the $j$-th fracture system, which indicates the contribution of the force direction to the activation of the fracture system. The term $\tau_i^{crit}/\min_i\tau_i^{crit}$ in Eq. (3) represents the contribution of the crystal plane's resistance to being plastically deformed, and the term $K_j^{IC}/\min_j K_j^{IC}$ in Eq. (4) represents the contribution of the crystal plane's resistance to being fractured. Figure 2 shows the resultant force $F_{result}$ during cutting, the crystal plane where the slip or fracture is activated, and the corresponding angles used in the equations for calculating the plastic deformation and cleavage fracture parameters. The $P$- and $F$-parameters are determined by the geometrical relationship between the direction

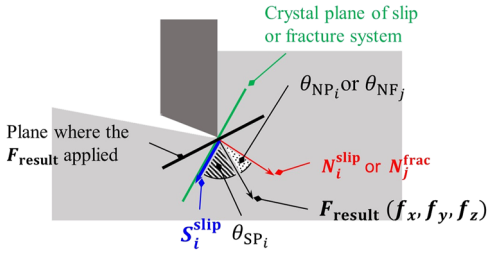


**FIG. 2.** Resultant force $F_{result}$ during the cutting process, and the angles used in the equations for calculating the plastic deformation and cleavage fracture parameters.

**TABLE II.** Fracture system of single-crystal sapphire.[17]

| Fracture system | Critical stress intensity factor (MPa m$^{0.5}$) |
|---|---|
| Basal fracture (C-plane) (0001) | 4.54 |
| Prismatic fracture (M-plane) {10$\bar{1}$0} | 3.14 |
| Rhombohedral fracture (R-plane) {$\bar{1}$012} | 2.38 |
| Prismatic fracture (A-plane) {11$\bar{2}$0} | 2.43 |

**TABLE I.** Slip/twinning system of single-crystal sapphire.[16]

| Slip (twinning) system | Miller–Bravais indices | Critical resolved shear stress (MPa) |
|---|---|---|
| Basal twinning (C-plane) | (0001) ⟨$\bar{1}$010⟩ | 2.2255 |
| Basal slip (C-plane) | (0001) ⟨11$\bar{2}$0⟩ | 2.2255 |
| Pyramidal slip | {0$\bar{1}$11}⟨10$\bar{1}$1⟩ | 4.4817 |
| Prismatic slip (A-plane) | {11$\bar{2}$0}⟨$\bar{1}$100⟩ | 1.6487 |
| Rhombohedral twinning (R-plane) | {$\bar{1}$012}⟨10$\bar{1}$1⟩ | 0.4066 |

of force and the slip/normal direction of the slip/fracture system. Because the cutting force is distributed differently along the interface between the tool and workpiece during the ultra-precision orthogonal cutting process, the parameters for plastic deformation and cleavage fracture should also be calculated on the basis of variations in force distribution. However, in this study, the distribution of the force is neglected, and the direction of the experimentally measured resultant force is assumed to be representative of the overall material removal behavior.

The critical resolved shear stress and critical stress intensity factor are listed in Tables I and II, respectively, with their related directionality in Miller–Bravais index form.

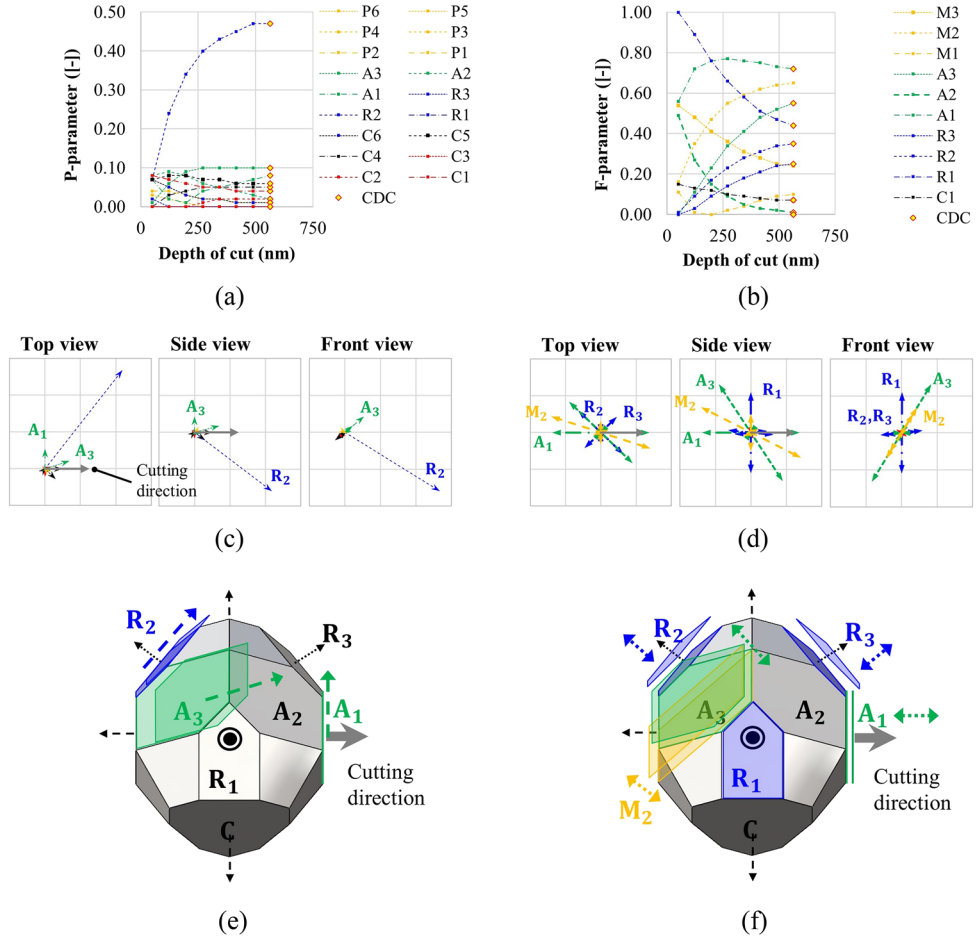


**FIG. 3.** Parameters of slip/fracture activation model for [$\bar{1}$120] cutting orientation on the R-plane (R180°) as examples. (a) and (b) Magnitudes of plastic deformation and cleavage fracture parameters, respectively, in terms of depth of cut. (c) and (d) Directions of plastic deformation and cleavage fracture parameters, respectively, at a specific depth of cut. (e) and (f) Illustrations of plastic deformation and cleavage fracture, respectively, based on a crystallographic view.

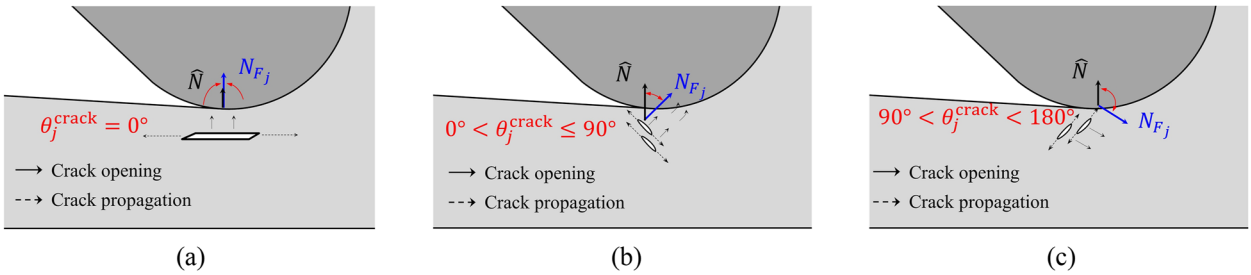


**FIG. 4.** Schematic of crack activation depending on the value of the fracture angle $\theta_j^{crack}$: (a) $\theta_j^{crack} = 0°$; (b) $0° < \theta_j^{crack} \leq 90°$; (c) $90° < \theta_j^{crack} < 180°$.

### B. Visualization of plastic deformation and cleavage fracture parameters

Both *P*- and *F*-parameters show vector characteristics, since they have both magnitude and direction. The magnitudes of the *P*- and *F*-parameters can be obtained from Eqs. (1) and (2), respectively. The direction of the *P*-parameter is the slip/twinning direction, while that of the *F*-parameter is the crack-opening direction, which is the same as the plane normal of the fracture system. Figures 3(a) and 3(b) show the *P*- and *F*-parameters, respectively, in terms of the depth of cut. CDC is the critical depth of cut, which denotes the depth of cutting at which cracks are initiated on the machined surface. Figures 3(c) and 3(d) show the visualized *P*- and *F*-parameters from the top, side, and front views. For a *P*-parameter, each grid denotes 0.1 both horizontally and vertically. For an *F*-parameter, each grid represents 0.2. Figures 3(e) and 3(f) show schematic views of the crystal structure and illustrate the slip/twinning and fracture activations, respectively, in the top view. All the indicated data are calculated from the R180° cutting orientation.

The direction of an *F*-parameter is quantified by defining a new parameter, namely, the fracture angle, which is the angle between the plane normal of the *j*-th fracture system and that of the cutting plane and can be expressed as follows:

$$\theta_j^{\text{crack}} = \arccos\left[\cos\left\{\left(N_{jx}^{\text{frac}}, N_{jz}^{\text{frac}}\right), \left(\hat{N}_x, \hat{N}_z\right)\right\}\right], \quad (5)$$

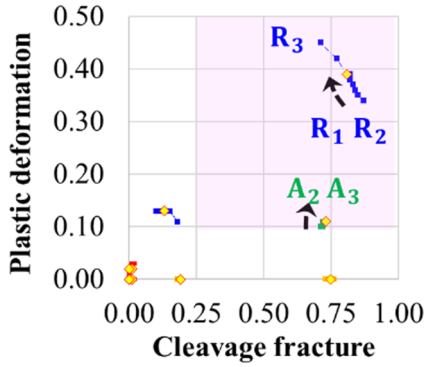


**FIG. 5.** P-parameter vs F-parameter for cases with R270° cutting orientation cases.

where $\left(N_{jx}^{\text{frac}}, N_{jy}^{\text{frac}}, N_{jz}^{\text{frac}}\right)$ are the coordinates of the plane normal of the *j*-th fracture system after the *z*-axis rotation of the coordinate system aligns the *x*-axis with the cutting direction, and $(\hat{N}_x, \hat{N}_y, \hat{N}_z)$ are those of the plane normal of the cutting plane. All coordinates are based on a Cartesian coordinate system. Figure 4 shows a schematic view of fracture activation in terms of $\theta_j^{\text{crack}}$. If $\theta_j^{\text{crack}}$ equals zero, the activated fracture opens parallel to the cutting surface [Fig. 4(a)]. If $\theta_j^{\text{crack}}$ is in the range $0° < \theta_j^{\text{crack}} \leq 90°$, the activated fracture opens in

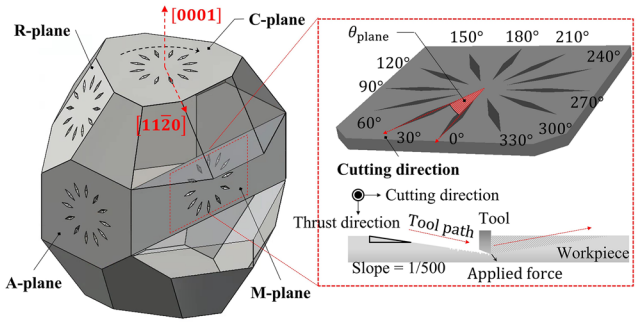


(a)

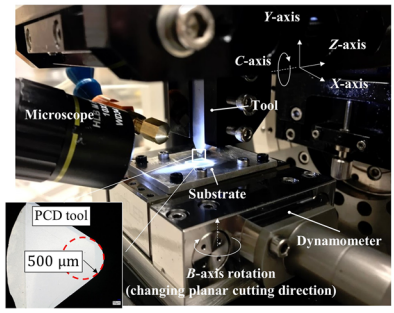


(b)

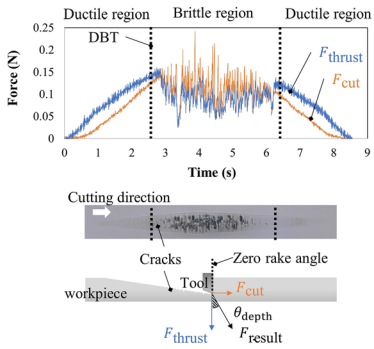


(c)

**FIG. 6.** (a) Schematic of the experiment. (b) Overall experimental setup. (c) Measured force data during ultra-precision orthogonal cutting.

the direction of the surface [Fig. 4(b)]. Finally, if $\theta_j^{crack}$ is in the range $90° < \theta_j^{crack} < 180°$, the activated fracture opens in the direction of the depth [Fig. 4(c)].

### C. Interactions between plastic deformation and cleavage fracture parameters

The mechanism responsible for some crack morphologies has been explained by coupling of plastic deformation and cleavage fracture parameter activations. It has been reported that a couple of high *P*- and *F*-parameters existing on the same crystal plane could affect the crack morphologies by simultaneous activation of plastic deformation and fracture.[15] In Ref. 15, it was also proposed that the generation of fan-shaped/spalling lateral cracks on the R180°, R210°, R240°, and R270° cutting orientations was due to the coupled effect of *P*- and *F*-parameters. The shapes of the crack boundaries and the directions of the step-like structures that appeared on the cracks were matched with the directions of the *F*- and *P*-parameters, respectively, on the same prismatic A-plane. The results of these observations implicitly reveal that coupling of simultaneously activated slip and fracture systems on the same crystal plane may significantly affect crack morphology.

Figure 5 shows the changes in the *P*-parameter in terms of the *F*-parameter on the same crystal plane for the R270° cutting orientation. Hereinafter, such graphs are called *PF* graphs. The yellow points with a red boundary indicate the data at the critical depth of cut. The different colors of the scatter denote different crystal plane cases. Furthermore, the data are scattered per depth of cut from 0 to the critical depth of cut (yellow point) with an ~5–10 nm increment as the cutting progresses. In the plot, the purple region indicates the domain of *P*- and *F*-parameters ranging from 25% to their maximum values. It has been hypothesized that the *PF* data in this box implicitly indicate that there may be an interaction between *P*-parameters and *F*-parameters with high probability. This purple region is defined as the interaction region. Observations of crack morphology in relation to the trend of the *PF* graph reveal that if the data passes through this purple region as cutting progresses, then spalling or fan-shaped lateral cracks are mainly created.

## III. EXPERIMENTAL SETUP

An orthogonal plunge cut was implemented on the C-, R-, A-, and M-planes of a sapphire substrate for various cutting orientations with 30° intervals along the clockwise direction as shown in Fig. 6(a). A 5 mm/min cutting speed was used, with a 1/500 slope. The cutting in each case was repeated three times to ensure repeatability. Figure 6(b) shows the experimental setup. A five-axis ultra-precision CNC machine, capable of 1 nm command resolution in the three linear axes and 1 $\mu$deg command resolution in the two rotary axes, was employed in conjunction with a binder-less nano-polycrystalline

**TABLE III.** Experimental setup.

| Item | Details |
|---|---|
| Crystal plane of substrate | C-, R-, A-, M-, 10 × 10 × 0.5 mm$^3$, Czochralski technique, polished, M.T.I Corporation, USA |
| Tool | Binder-less nano-polycrystalline tool, 0.5 mm nose radius, 0° rake angle, 9° clearance angle, A.L.M.T. Corporation, Japan |
| Machine | ROBONANO α-0*i*B, FANUC Corporation, Japan |
| Dynamometer | Type 9119AA1, KISTLER Instrument Corporation, Switzerland |
| Amplifier | With 5000 Hz low-pass filter, type 50800A, KISTLER Instrument Corporation, Switzerland |
| Coolant | Mineral oil-based coolant (Japan) |
| Cutting speed (feed rate) | 5 mm/min with 1/500 slope |
| Cutting orientations | Seven directions for each crystal plane, considering symmetry. 30° interval along clockwise direction. C- and R-planes: 90°, 120°, 150°, 180°, 210°, 240°, 270° (0° is $[11\bar{2}0]$), A- and M-planes: 0°, 30°, 60°, 90°, 120°, 150°, 180° (0° is [0001]) |

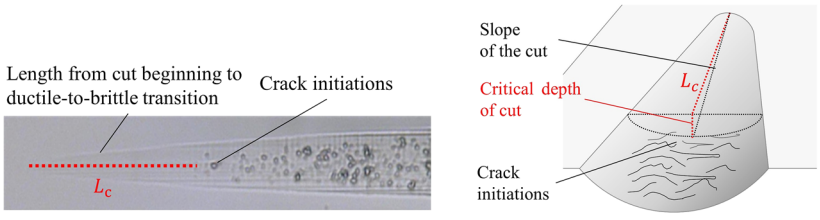


**FIG. 7.** Calculating critical depth of cut from experimental data.

diamond tool featuring a 0.5 mm nose radius and a 500 nm edge radius. The cutting force and thrust force were measured by a piezoelectric dynamometer on which the substrate was mounted. The flatness of the workpiece was adjusted by a tilt stage and surface probe. An optical microscope was used to establish the tool–work contact. Figure 6(c) shows the measured force during the orthogonal ultra-precision machining of sapphire. When the increasing depth of cut does not approach the critical depth of cut, the measured cutting force and thrust force are stable, but they become unstable and oscillate when the depth of cut exceeds the critical value. The experimental conditions and information about the setup are summarized in Table III. The crack morphologies at ductile-to-brittle transition on the machined surface were captured using an optical microscope and scanning electron microscope (SEM; Leo 1530, ZEISS Corp.). Micro-optics (VHX-5000, Keyence Corp.) was used with ×500 magnification to determine the critical depth of cut, i.e., the depth at which the ductile-to-brittle transition occurred. The length from the beginning of the cutting to the ductile-to-brittle transition was measured, and this was converted to the critical depth of cut by multiplying by the sine of the slope of the cut, as shown in Fig. 7.

## IV. RESULTS AND DISCUSSION

### A. Measurement of critical depth of cut

Figure 8 shows the critical depth of cut for various cutting planes and cutting orientations. The crack images captured by SEM are also shown for each cutting orientation case. The values of the critical depth of cut and the shapes of the crack morphology show symmetric distributions along a line with direction [$1\bar{1}00$] for the C- and R-planes and direction [0001] for the A- and M-planes (red dashed line). Because of this, among 12 total cutting orientation cases, only seven cut directions were used in the study: the C- and R-plane cases used cutting orientations from 90° to 270° with a 30° increment, and the A- and M-plane cases used cutting orientations from 0° to 180° with a 30° increment.

### B. Analysis of crack morphology

On the basis of the SEM observations, the crack morphologies at the ductile-to-brittle transition were broadly categorized into three shapes: sculptured, layered, and spalling/fan-shaped lateral cracks. The crack morphologies were analyzed in relation to the magnitude and direction of *P*- and *F*-parameters and their interactions. Figure 9 shows the schematic views of each crack morphology and the related morphologies captured by SEM.

A layered crack has a morphology indicating that the layer parallel to the cutting surface has been torn off. The depth of the crack is shallow compared with other types of cracks. A sculptured crack has valley-like structures with a clear boundary. Lateral cracks can be divided into spalling cracks and fan-shaped cracks according to the degree of crack development. If this is low, then a spalling crack can be observed, looking as if it was dug by a shovel. If the development degree is large, then the crack appears to have propagated in the radial direction up a certain point and torn off, giving it a fan-like appearance.

Figure 10 shows the crack morphologies when the C-plane is used as the cutting plane. Clear lamellar sculptured cracks can be

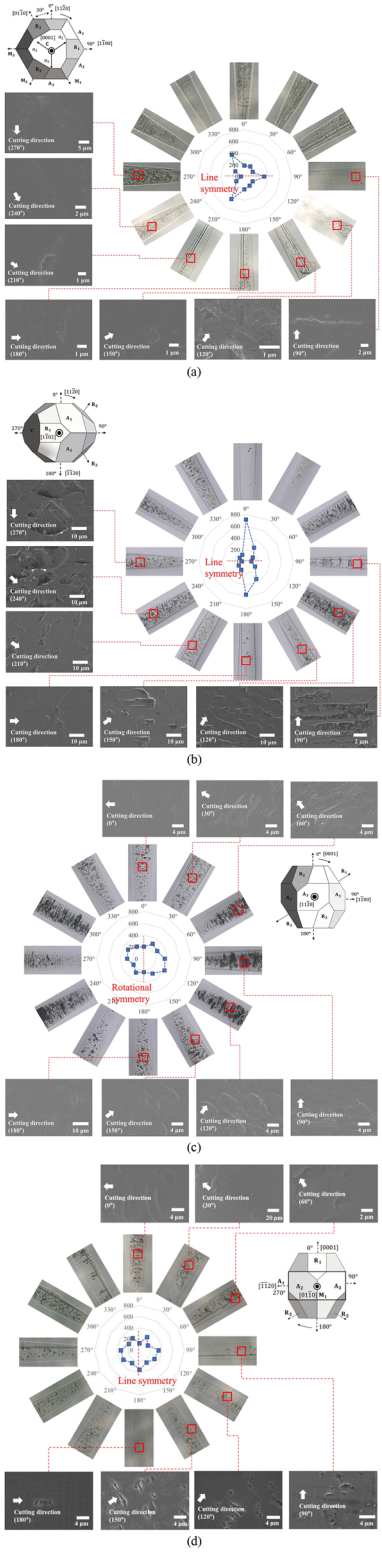


**FIG. 8.** Critical depth of cut and crack morphologies of (a) C-, (b) R-, (c) A-, and (d) M-planes.

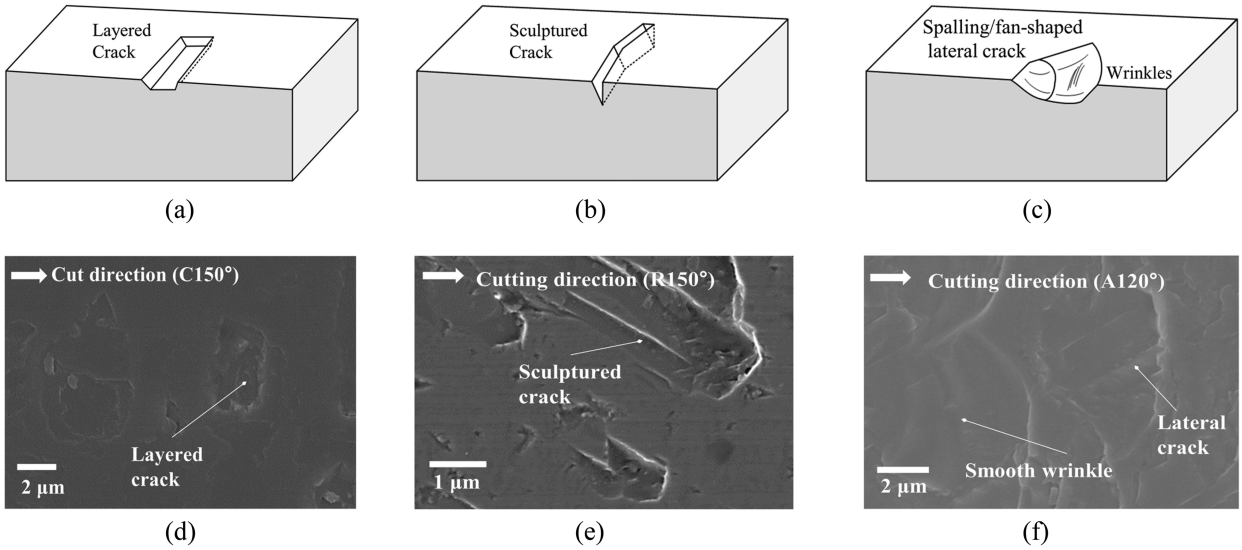


**FIG. 9.** Categorization of crack: schematic views of (a) layered crack, (b) sculptured crack, and (b) lateral crack, together with crack morphologies from SEM related to (d) layered crack observed at C150° cutting orientation, (e) sculptured crack observed at R150° cutting orientation, and (f) lateral crack observed at A120° cutting orientation.

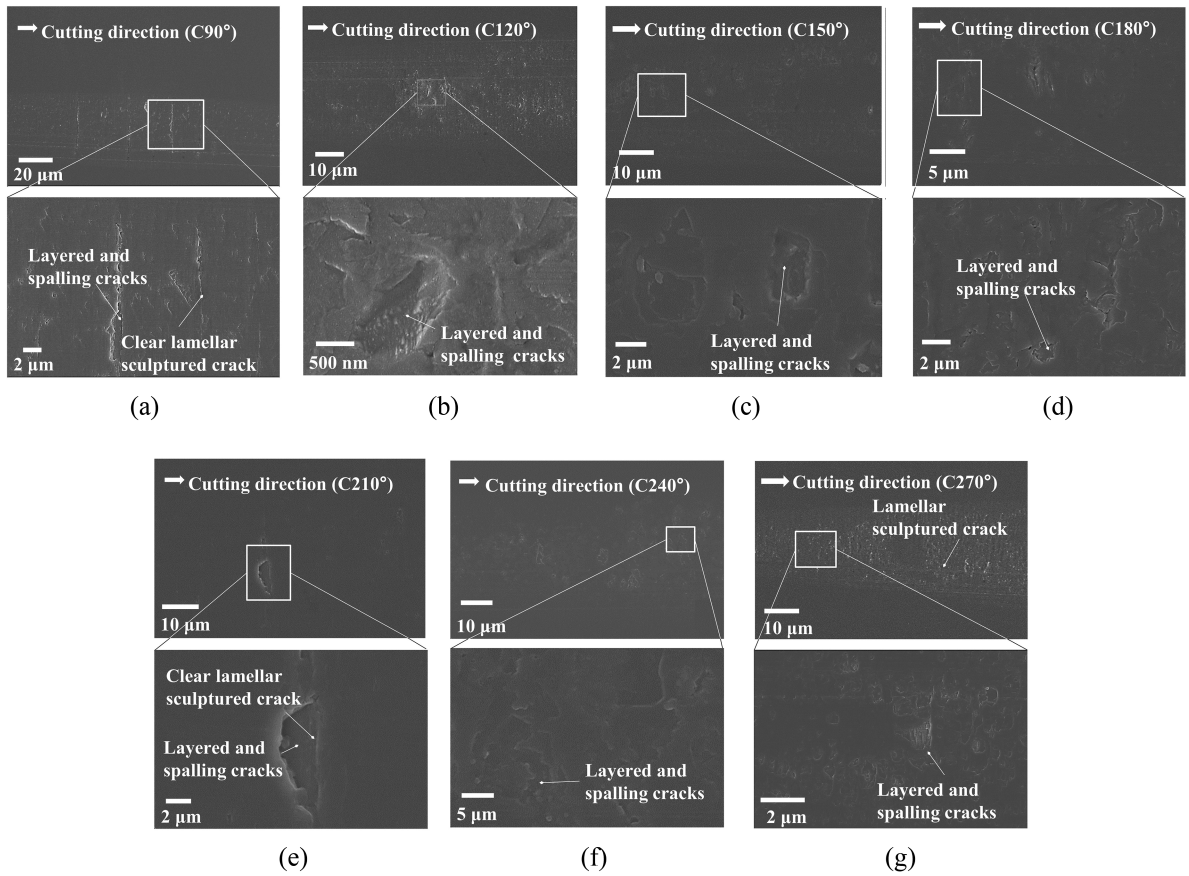


**FIG. 10.** Crack morphologies captured by SEM for (a) C90°, (b) C120°, (c) C150°, (d) C180°, (e) C210°, (f) C240°, and (g) C270° C-plane cutting orientations.

observed at the C90° and C210° cutting orientations. For other cutting orientations, overall similar crack morphologies can be found. The shallow layered cracks are mostly observed, with some of the layered cracks showing a combination of spalling and layered cracks.

Figure 11 shows schematics of the *F*-parameters in top views and the vector form of the *F*-parameters in side views for the C-plane case. The side views of the visualized *F*-parameters are almost the same for all cutting orientations: there are highly activated rhombohedral R-fractures (blue arrows) with $\theta_j^{\text{crack}}$ values ranging between 122.3° and 142.4° and basal C-fractures (red arrows) with a $\theta_j^{\text{crack}}$ value of zero. Prismatic A- and M-planes with a $\theta_j^{\text{crack}}$ of 90° are also found.

The crack morphologies together with spalling and layered cracks can be explained by both rhombohedral R-fractures and the basal C-fracture. If the crack-opening direction points in the depth direction, as with the rhombohedral fractures observed in all C-plane cases, then a lateral crack can develop. Simultaneously, basal C-fractures create layered cracks that are parallel to the cutting plane. Consequently, a crack morphology comprising a spalling crack and a layered crack can be formed. For the C90°, C150°, C210°, and C270° cutting orientations, lamellar sculptured cracks are found. This is because of the relatively highly activated prismatic M-fractures in these directions. The $\theta_j^{\text{crack}}$ of the prismatic M-fractures is 90°, and the plane normal is parallel to the cutting

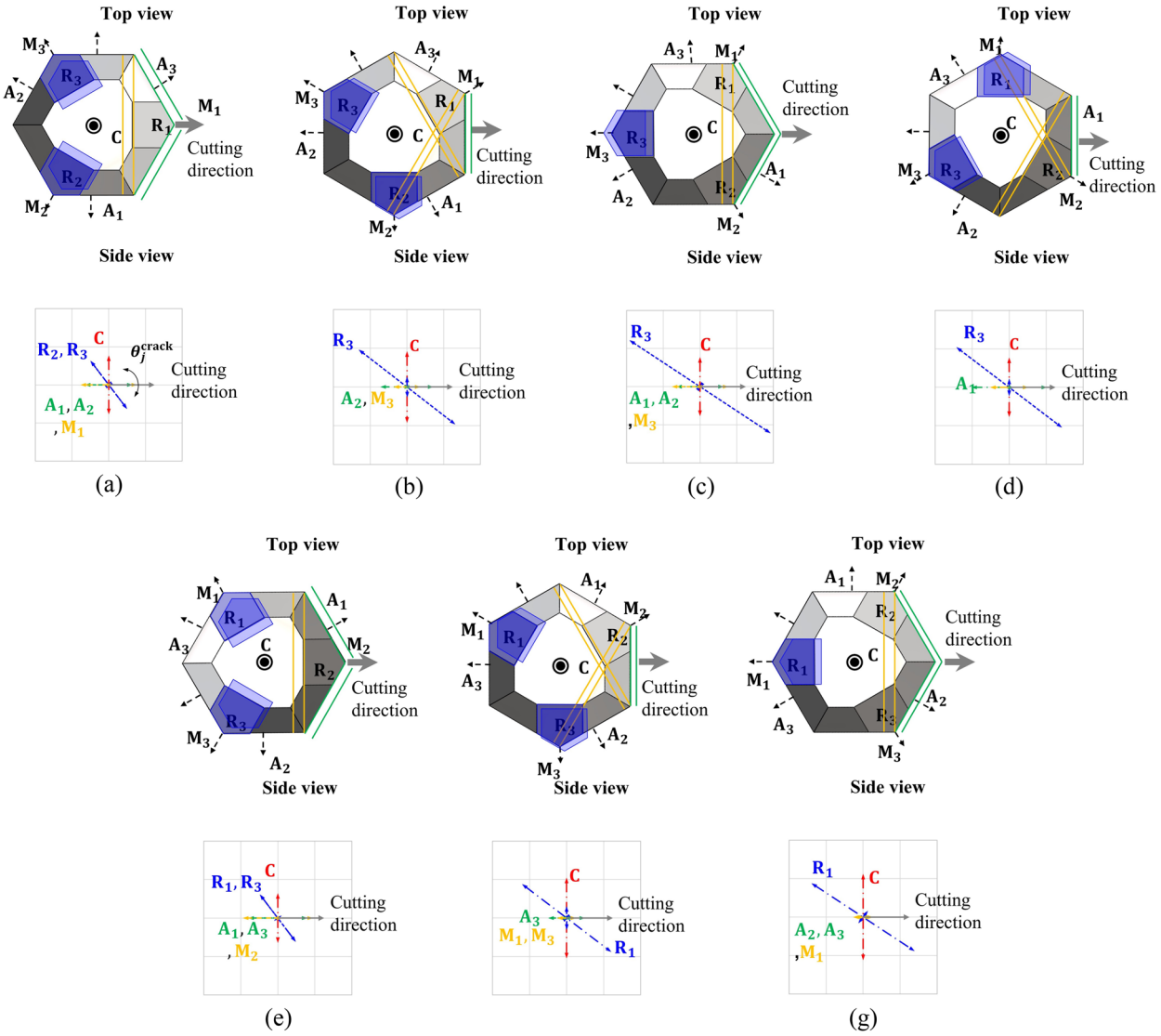


**FIG. 11.** Visualized *F*-parameters for (a) C90°, (b) C120°, (c) C150°, (d) C180°, (e) C210°, (f) C240°, and (g) C270° C-plane cutting orientations.

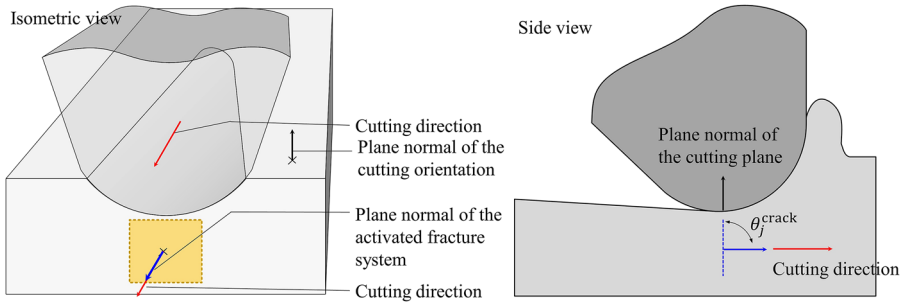


**FIG. 12.** Mechanism of lamellar sculptured crack: $\theta_j^{crack} = 90°$, and the plane normal is parallel to the cutting orientation.

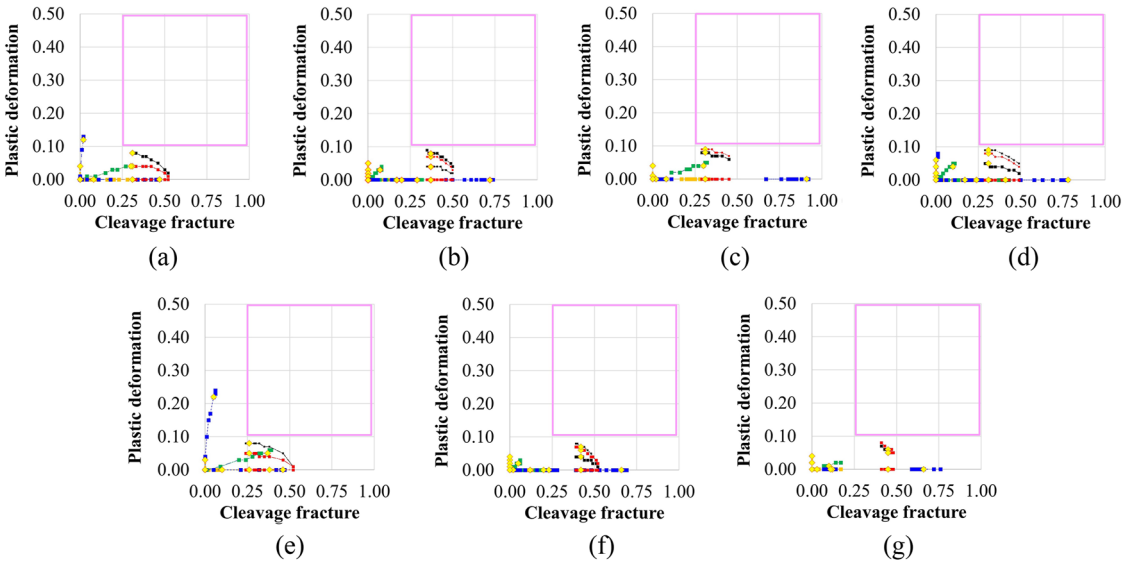


**FIG. 13.** Graphs of *P*-parameter vs *F*-parameter for (a) C90°, (b) C120°, (c) C150°, (d) C180°, (e) C210°, (f) C240°, and (g) C270° cutting orientations when the C-plane is used as the cutting plane.

orientation, as shown in Fig. 12. When the crack propagations reach the machined surface, a lamellar sculptured crack can be generated.

Furthermore, the effect of coupled *P*- and *F*-parameters on crack morphologies for the C-plane case is investigated. Figure 13 shows the *PF* graphs on the C-plane for seven cutting orientations. As can be seen, for none of the cutting orientations show the data pass through the interaction region outlined by the purple box. According to the interpretation of interactions based on *PF* graphs, this means that with the C-plane as the cutting plane, interactions between *P*- and *F*- parameters rarely occur.

Figure 14 shows the crack morphologies when the R-plane is used as the cutting plane. It can be seen that the various shapes of the cracks depend on the cutting orientation. For the R90°, R120°, and R150° cutting orientations, crack morphologies with linear shapes can clearly be observed [red lines in Figs. 14(a)–14(c)]. However, a layered crack is found in the R90° case, while only sculptured cracks can be found at the R120° cutting orientation. Furthermore, the R150° case shows a hybrid crack, comprising both sculptured and spalling cracks [Fig. 15(a)]. As the cutting orientation changes from R150° to R270°, the predominant form of crack gradually changes from sculptured to spalling and fan-shaped lateral. For the R240° and R270° cases, a second hybrid crack consisting of not only a fan-shaped lateral crack but also a layered crack is also observed [Fig. 15(b)].

Figure 16 shows schematics of the *F*-parameters in top views and the vector form of the *F*-parameters in side views for the R-plane case. For the R90° and R120° cutting orientations, there are multiple activations of fracture systems; however, only the basal C-fracture has a $\theta_j^{crack}$ of 122.5° and 125.6° and crack-opening directions pointing in the depth direction. The crack-opening directions of all other fracture systems have $\theta_j^{crack}$ evenly distributed in the range $0° < \theta_j^{crack} < 90°$. The $\theta_j^{crack}$ values of prismatic A2-, A3- and prismatic M1-fractures for the R90° case are 57.3° and 58.0°, respectively. Moreover, the $\theta_j^{crack}$ values of rhombohedral

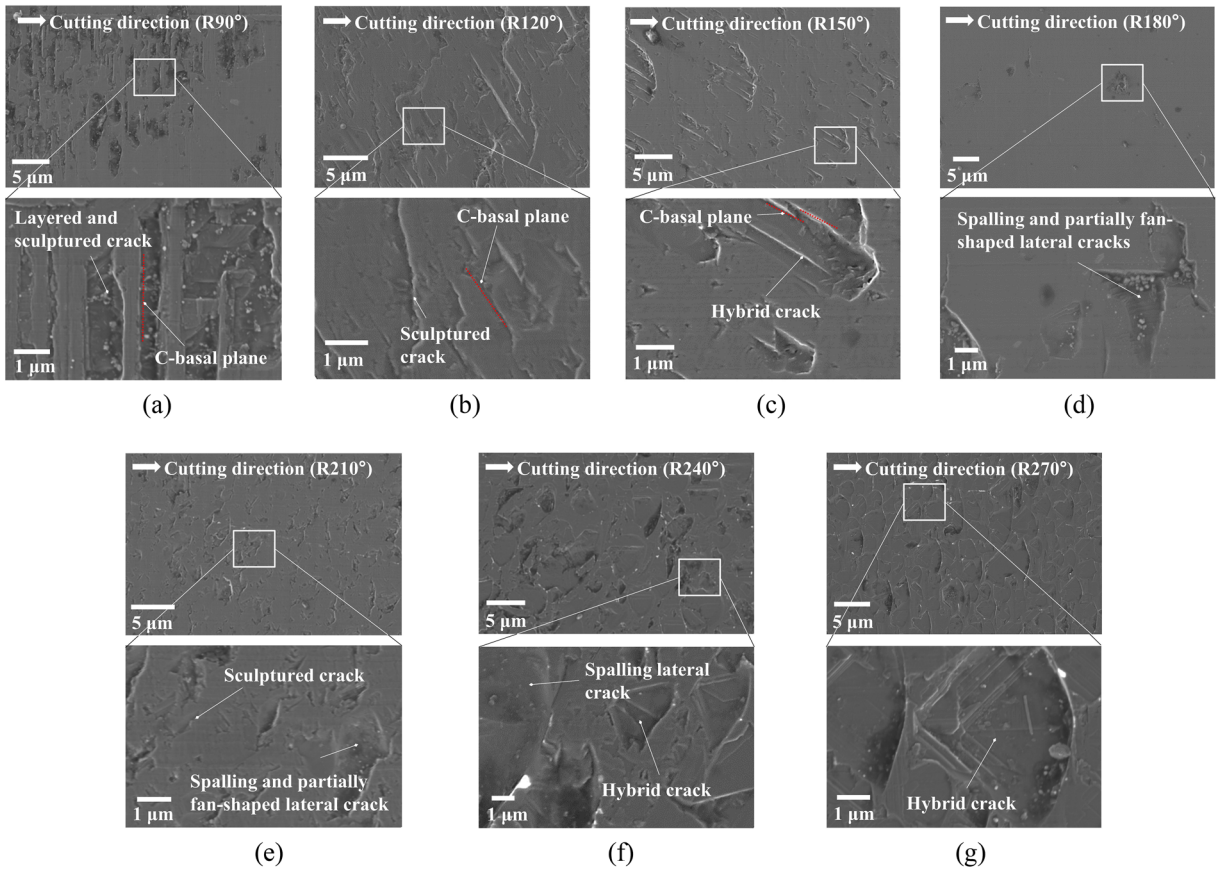


**FIG. 14.** Crack morphologies captured by SEM for (a) R90°, (b) R120°, (c) R150°, (d) R180°, (e) R210°, (f) R240°, and (g) R270° R-plane cutting orientations.

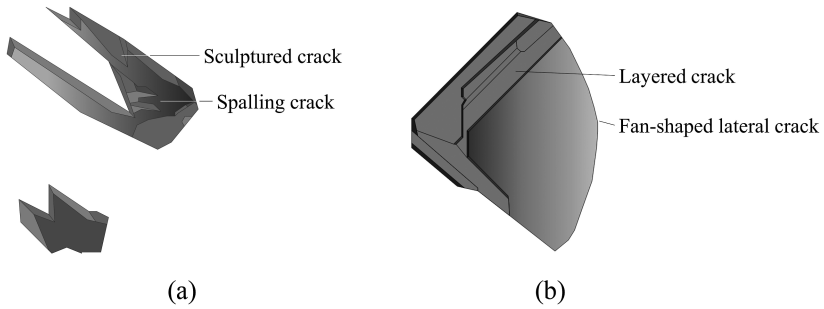


**FIG. 15.** Schematics of (a) first hybrid cracks appearing at R150° orientation and (b) second hybrid crack appearing at R240° and R270° orientations.

R3- and prismatic A3-fractures for the R120° case are 84.8° and 11.3°, respectively. All these have crack-opening directions pointing in the surface direction. When the direction of crack-opening points in the cutting-surface direction, there is relatively rapid removal of material in front of the crack-initiation region, generating a deep valley to create a sculptured crack. The observation of sculptured cracks can be explained by these fracture activations.

In Fig. 16(c), the multiple fracture activations and $\theta_j^{\text{crack}}$ values are widely distributed: 0° (R1), 16.7° (M1), 90° (A1), 126° (M2), 140.2° (C), and 165.3° (A3). R150° reveals hybrid cracks, with both sculptured and spalling lateral cracks being created simultaneously. Figures 16(d)–16(g) show that the $F$-parameter of the prismatic A-fracture, which opens toward the depth direction, is dramatically increased, possibly leading to the development of fan-shaped

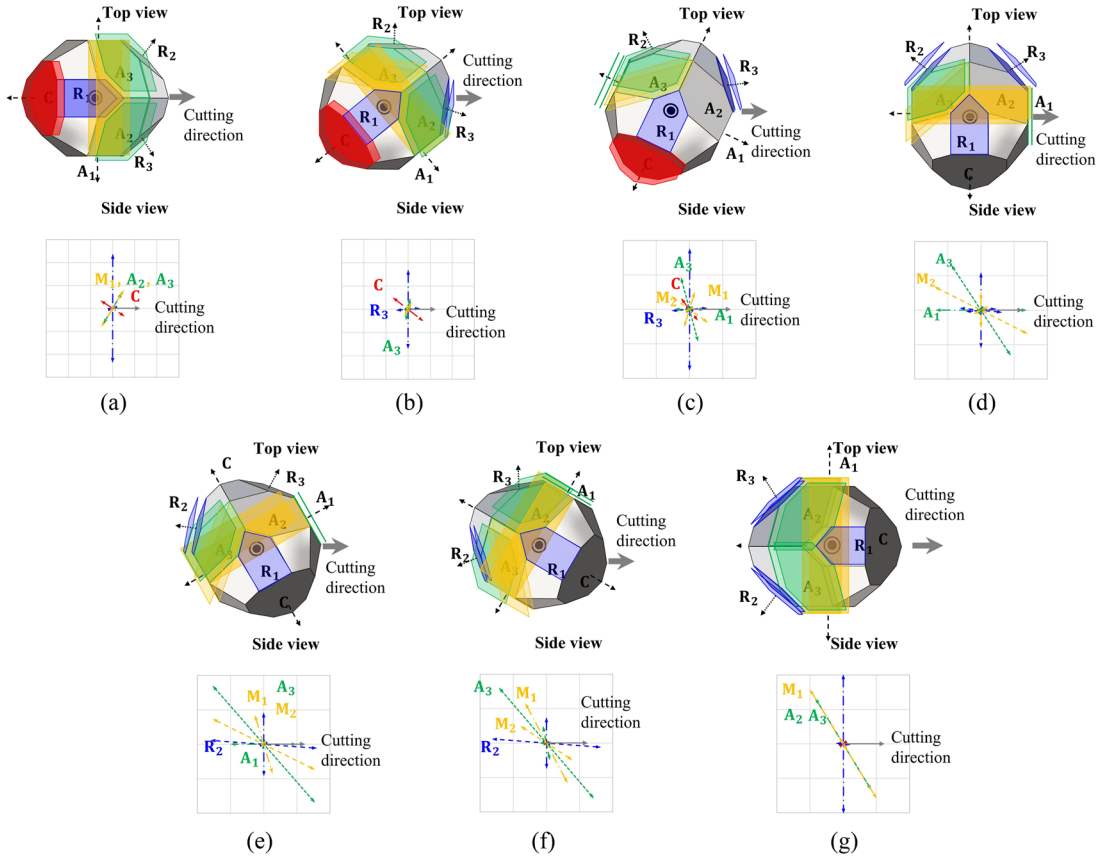


**FIG. 16.** Visualized *F*-parameters for (a) R90°, (b) R120°, (c) R150°, (d) R180°, (e) R210°, (f) R240°, and (g) R270° R-plane cutting orientations.

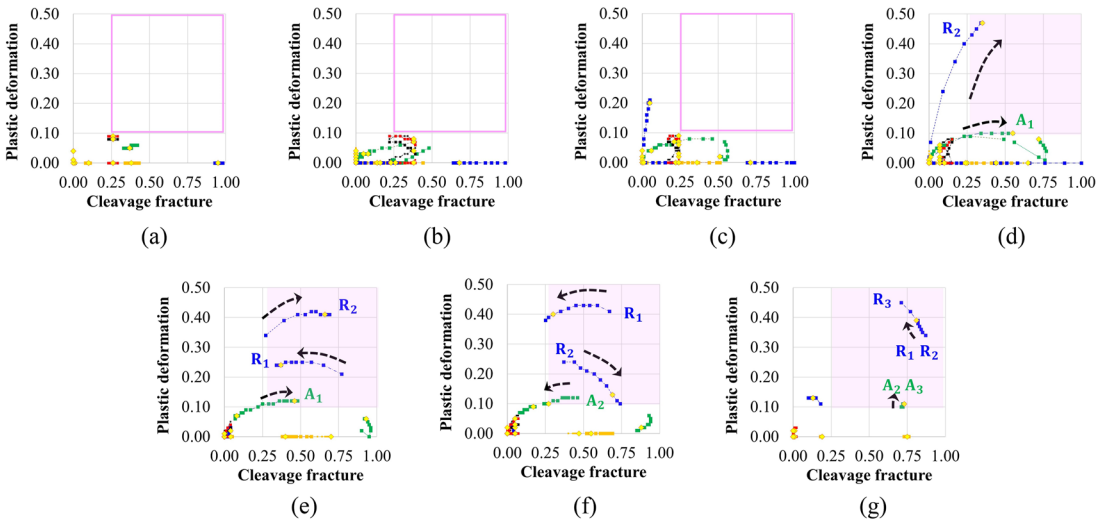


**FIG. 17.** Graphs of *P*-parameter vs *F*-parameter for (a) R90°, (b) R120°, (c) R150°, (d) R180°, (e) R210°, (f) R240°, and (g) R270° cutting orientations when the R-plane is used as the cutting plane.

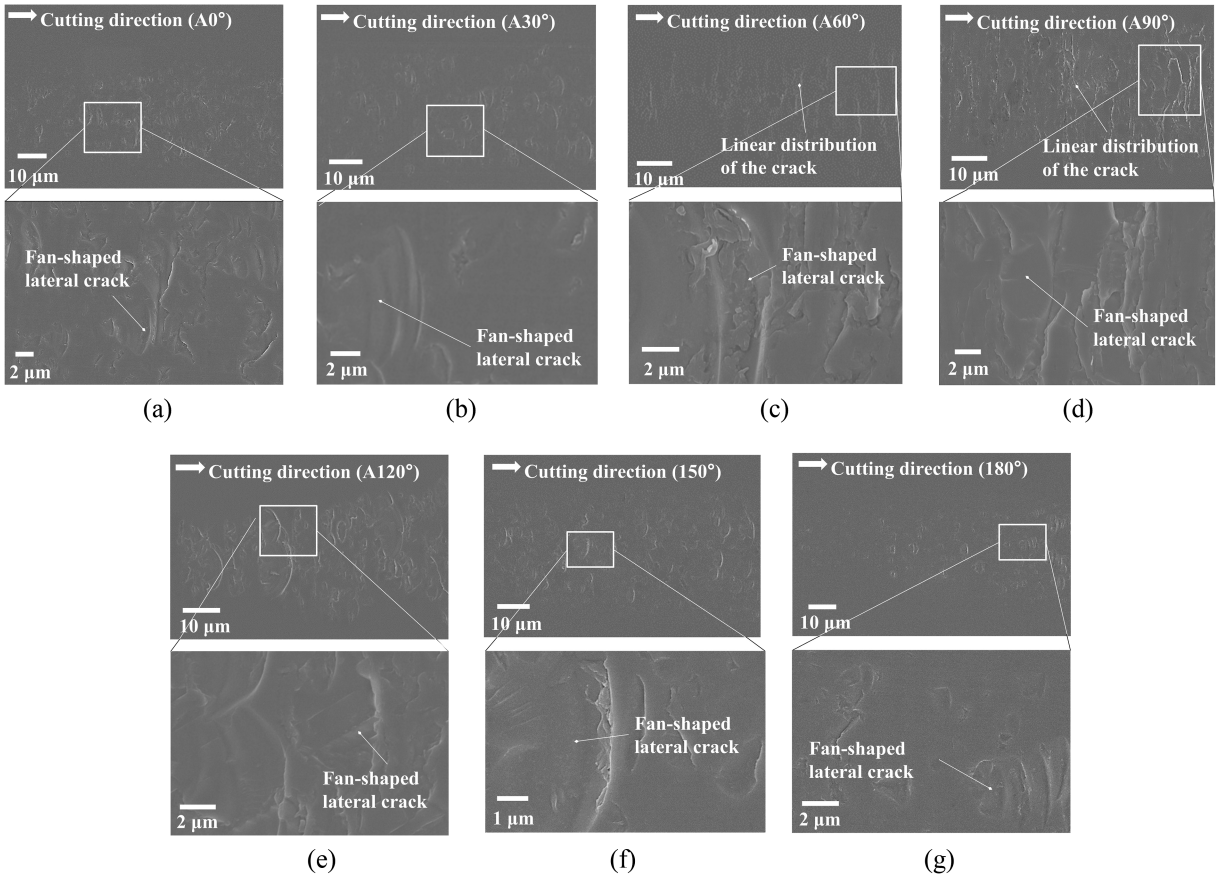


**FIG. 18.** Crack morphologies captured by SEM for (a) A0°, (b) A30°, (c) A60°, (d) A90°, (e) A120°, (f) A150°, and (g) A180° A-plane cutting orientations.

lateral cracks. In addition, as the *F*-parameter of the rhombohedral R1-plane is also dramatically increased, a hybrid crack comprising a fan-shaped lateral and a layered crack is created.

Figure 17 shows the *PF* graphs on the R-plane for seven cutting orientations. Here, the R180°, R210°, R240°, and R270° cases show that the data for the rhombohedral R-plane and prismatic A-plane pass through the interaction region. This means that during the ultra-precision machining process on the R-plane, these four cutting orientations may cause strong interactions in both the prismatic A-plane and rhombohedral R-plane. As shown in Fig. 14, these R180°, R210°, R240°, and R270° cases for which the possibility of interactions is indicated all exhibit spalling or fan-shaped lateral cracks on the machined surface. Thus, the *PF* interactions may accelerate lateral crack development.

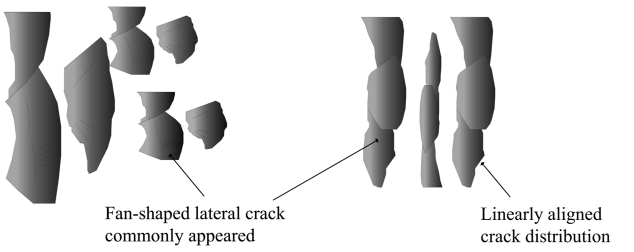


**FIG. 19.** Fan-shaped lateral cracks distributed along the line perpendicular to the cutting orientation.

Figure 18 shows the crack morphologies when the A-plane is used as the cutting plane. Overall, fan-shaped lateral cracks mainly appear in the A-plane cases. In particular, the A60° and A90° cases both show fan-shaped lateral cracks distributed along the line perpendicular to the cutting orientation (Fig. 19).

Figure 20 shows schematics of the *F*-parameters in top views and the vector form of the *F*-parameters in side views for the A-plane case. For all cutting orientations, there are highly activated fractures with opening direction toward the depth direction, and except for the A0° and A180° cases, all the cutting orientations have multiple fractures of this type. The A60° and A90° cases have a highly activated rhombohedral R1-fracture and a prismatic M1-fracture, respectively, with $\theta_j^{\text{crack}} = 90°$ and their plane normal parallel to the cutting plane, as in the C90° case shown in Fig. 12. The linear distribution of the cracks observed in the A60° and A90° cutting orientations can be explained by these activations.

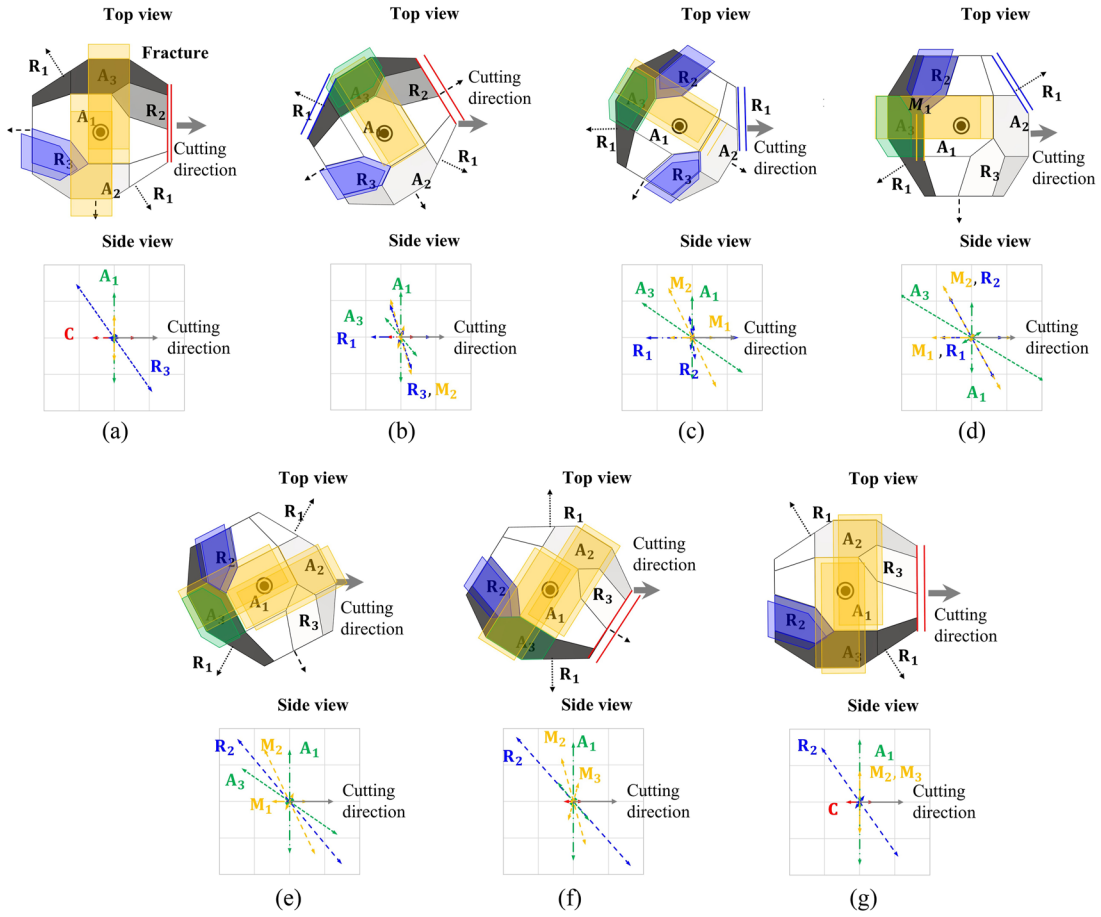


**FIG. 20.** Visualized *F*-parameters for (a) A0°, (b) A30°, (c) A60°, (d) A90°, (e) A120°, (f) A150°, and (g) A180° A-plane cutting orientations.

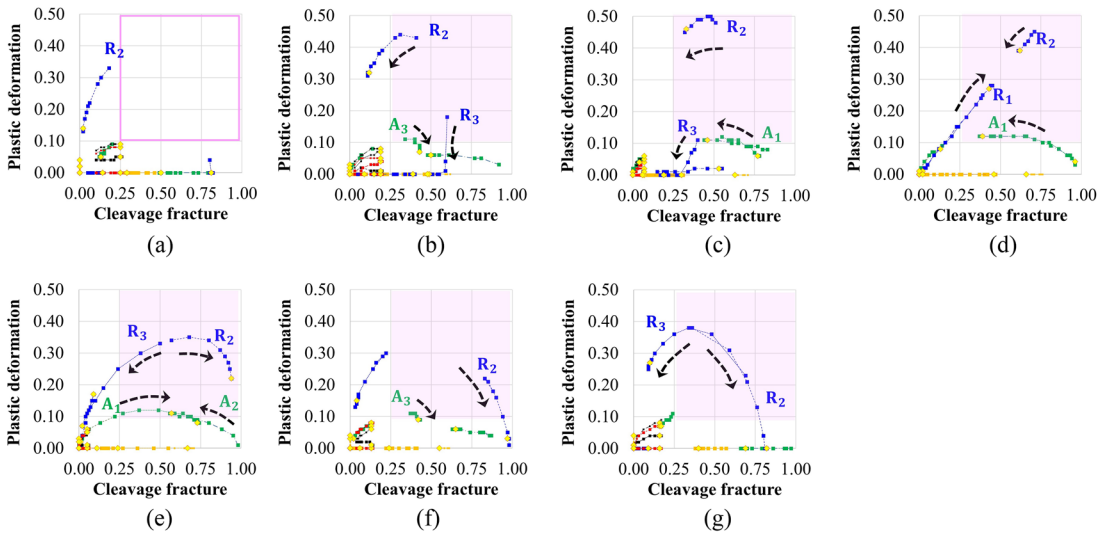


**FIG. 21.** Graphs of *P*-parameter vs *F*-parameter for (a) A0°, (b) A30°, (c) A60°, (d) A90°, (e) A120°, (f) A150°, and (g) A180° cutting orientations when the A-plane is used as the cutting plane.

Figure 21 shows the *PF* graphs on the A-plane for seven cutting orientations. For all the cutting orientations except the A0° case, the *PF* data from the rhombohedral R- and prismatic A-planes pass through the interaction region, indicating the presence of interactions from multiple crystal planes, rhombohedral R-planes, and prismatic A-planes, which can explain the crack observations in Fig. 18, which reveal mainly fan-shaped lateral cracks. For the A0° orientation, the *PF* data of the second rhombohedral R-plane ($R_2$) are very close to the interaction region. If data tolerance is taken into account, it may be supposed that even the A0° case involves high interactions on the second rhombohedral R-plane, which could explain the fan-shaped lateral crack in this case.

Figure 22 shows the crack morphologies when the M-plane is used as the cutting plane. The M0°, M30°, M60°, and M90° cutting orientations [Figs. 22(a)–22(c)] all show fan-shape lateral cracks similar to the A-plane case. The M120°, M150°, and M180° orientations show hybrid cracks comprising spalling lateral, partially fan-shaped lateral, and sculptured cracks.

Figure 23 shows schematics of the *F*-parameters in top views and the vector form of the F-parameters in side views for the M-plane case. For the M0° to M90° cutting orientations, the highly activated fractures mostly have $\theta_j^{\text{crack}}$ in the range $90° < \theta_j^{\text{crack}} < 180°$. However, for the M120°, M150°, and M180° cases, there are also highly activated fractures with $\theta_j^{\text{crack}}$ in the range $0° < \theta_j^{\text{crack}} < 90°$. The M120° case has a highly activated prismatic A2-fracture with $\theta_j^{\text{crack}} = 24.8°$ and a rhombohedral R1-fracture with $\theta_j^{\text{crack}} = 24.8°$. The M150° case has a highly activated prismatic A2-fracture with $\theta_j^{\text{crack}} = 15.5°$, a rhombohedral R1-fracture with $\theta_j^{\text{crack}} = 15.5°$, and a rhombohedral R1-fracture with $\theta_j^{\text{crack}} = 26.6°$. The M180° case has a highly activated rhombohedral R1-fracture with $\theta_j^{\text{crack}} = 33.7°$. These results can explain the presence of hybrid cracks that are combinations of spalling cracks, partially fan-shaped cracks, and sculptured cracks.

Figure 24 shows the *PF* graphs on the M-plane for seven cutting orientations. Similar to the A-plane case, for all the cutting orientations except the M0° case, the *PF* data from the rhombohedral R- and prismatic A-planes pass through the interaction region. These *PF* graphs indicate the presence of interactions from multiple crystal planes, rhombohedral R-planes, and prismatic A-planes, which can explain the crack observations shown in Fig. 22, revealing mainly spalling lateral cracks and fan-shaped lateral cracks. For the M0° case, the *F*-parameter of the first rhombohedral R-plane ($R_1$) is extremely high, and, from Fig. 23, $\theta_j^{\text{crack}}$ of this activation is

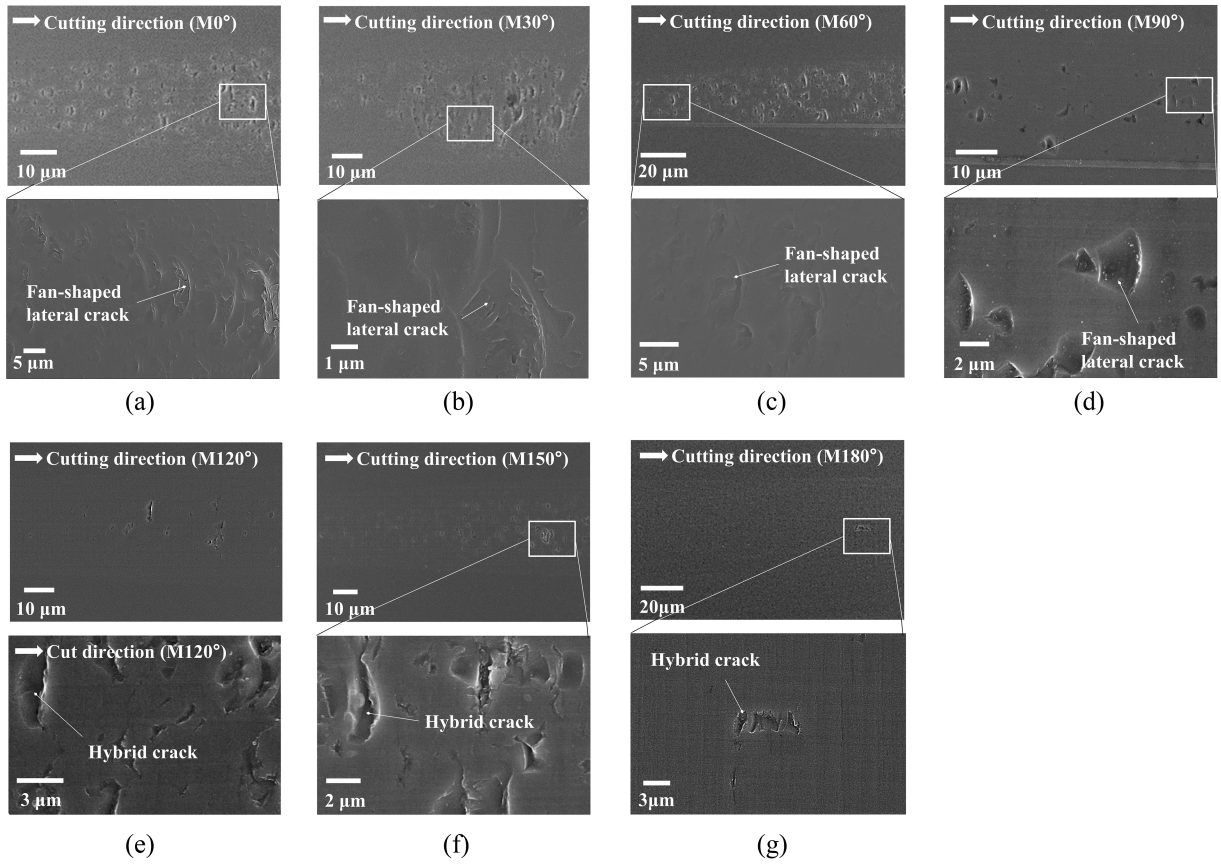


**FIG. 22.** Crack morphologies captured by SEM for (a) M0°, (b) M30°, (c) M60°, (d) M90°, (e) M120°, (f) M150°, and (g) M180° M-plane cutting orientations.

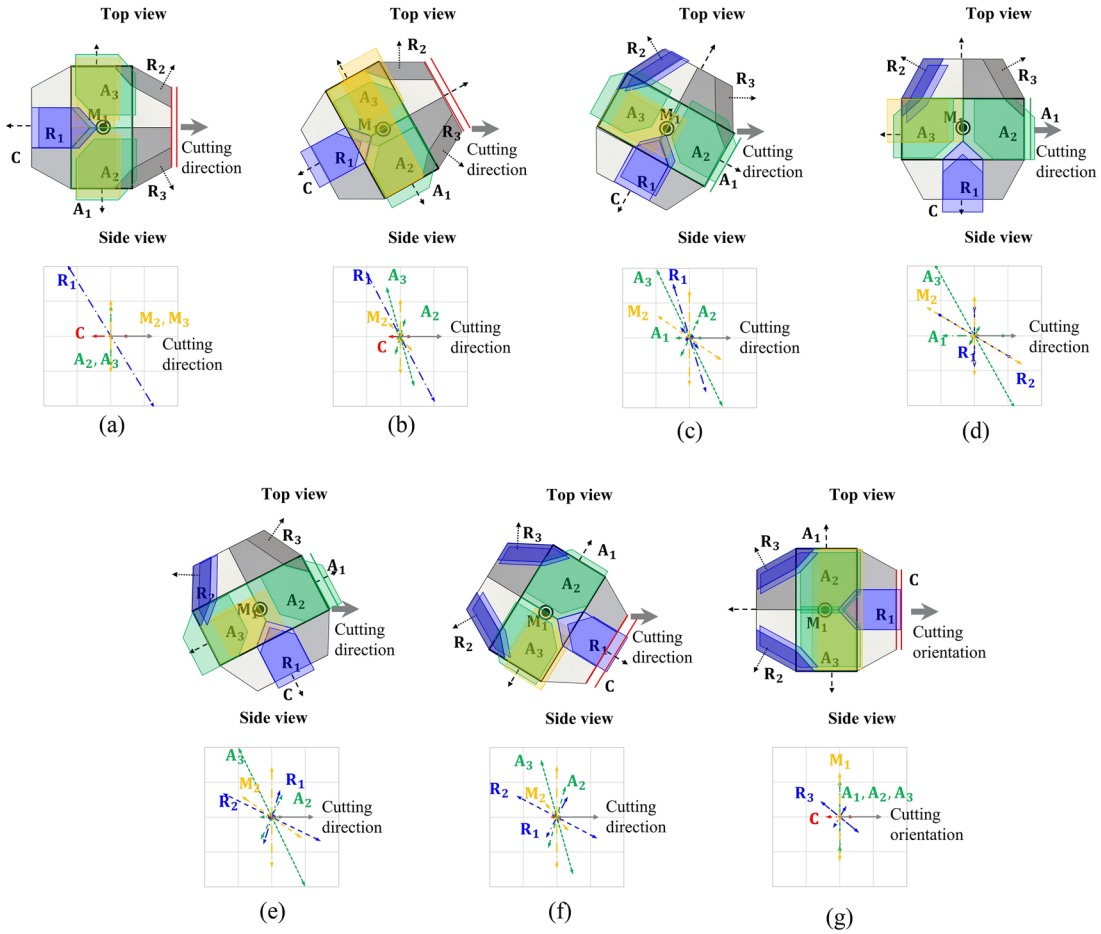


**FIG. 23.** Crack morphologies captured by SEM for (a) M0°, (b) M30°, (c) M60°, (d) M90°, (e) M120°, (f) M150°, and (g) M180° M-plane cutting orientations.

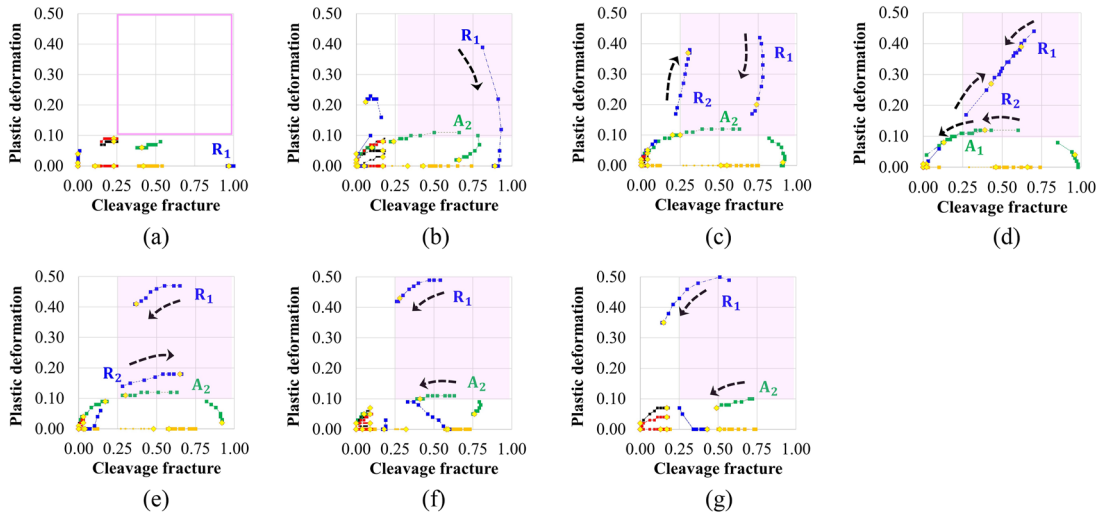


**FIG. 24.** Graphs of *P*-parameter vs *F*-parameter for (a) M0°, (b) M30°, (c) M60°, (d) M90°, (e) M120°, (f) M150°, and (g) M180° cutting orientations when the M-plane is used as the cutting plane.

**TABLE IV.** Summary of crack morphology characteristics for the C-, R-, A-, and M-planes, together with the corresponding *PF* parameters.

| Cutting orientation | Crack morphologies, related plastic deformation, and cleavage fracture parameters |
|---|---|
| C90° and C210° | Layered crack and spalling lateral crack (combination of rhombohedral R-fracture and basal C-fracture), clear lamellar sculptured crack (prismatic M-fracture) |
| C120°, C180°, and C240° | Layered crack and spalling lateral crack (combination of rhombohedral R-fracture and basal C-fracture) |
| C150° and C270° | Layered crack and spalling lateral crack (combination of rhombohedral R-fracture and basal C-fracture), lamellar sculptured crack (prismatic M-fracture) |
| R90° | Layered crack and lamellar sculptured crack (combination of prismatic A-, prismatic M-, and rhombohedral R-fractures), linear sculptured crack (by C-fracture) |
| R120° | Sculptured crack (combination of prismatic A-, prismatic M-, and rhombohedral R-fractures), linear sculptured crack (by C-fracture) |
| R150° | First hybrid crack: Sculptured crack and spalling lateral crack (various directions of fracture activation), linear sculptured crack (by C-fracture) |
| R180° and R210° | Spalling lateral crack and partially fan-shaped lateral crack (by *PF* interactions) |
| R240° and R270° | Second hybrid crack: Layered crack and fan-shaped lateral crack (by multiple fractures and *PF* interactions) |
| A0°, A30°, A120°, A150°, and A180° | Fan-shaped lateral crack (by *PF* interactions) |
| A60° and A90° | Fan-shaped lateral crack with linear distribution (by *PF* interactions and fracture activations parallel to cutting orientations) |
| M0°, M30°, and M60° | Fan-shaped lateral crack (by *PF* interactions) |
| M90°, M120°, M150°, and M180° | Third hybrid crack: Sculptured crack, spalling lateral crack, and partially fan-shaped lateral crack (by fracture activations in various directions and *PF* interactions) |

147.6°, in the range $90° < \theta_j^{crack} < 180°$. It may be considered that even though interactions are almost absent in the M0° case, spalling lateral cracks are still created because of the extremely high value of the *F*-parameter on the first rhombohedral R-plane in this case.

Table IV summarizes the characteristics of the observed crack morphologies, plastic deformation, and cleavage fracture parameters for the C-, R-, A-, and M-planes.

## V. CONCLUSION

In this work, the mechanism of crack generation during ultra-precision machining of single-crystal sapphire has been studied in terms of various crystal planes and cutting orientations. On the basis of SEM observations of cracks, the crack morphologies have been categorized into three types: sculptured, layered lateral, and spalling/fan-shaped lateral cracks. Plastic deformation and cleavage fracture parameters have been calculated using a modified slip/fracture activation model to analyze the crack-generation mechanism in relation to the crystallographic properties of sapphire.

The mechanism of crack generation has been investigated from two perspectives: the directionality of the cleavage fracture parameter, and the presence of interactions between the plastic deformation and cleavage fracture parameters. To enable quantitative analysis, the angle between the cutting plane and the fractured crystal plane, $\theta_j^{crack}$, was considered. To determine the probability of interaction between the plastic deformation and cleavage fracture parameters, *PF* plots were generated in which the interaction zone was defined as the domain of *P*- and *F*-parameters ranging from 25% to their maximum values. Analysis revealed that if spalling or fan-shaped lateral cracks appeared, $\theta_j^{crack}$ was in the range $90° < \theta_j^{crack} < 180°$ and data in the *PF* plots for any crystal plane passed through the interaction zone.

The current study has been performed with a measured force. For a more accurate understanding and to enable predictions regarding the critical depth of cut and crack morphologies, a stress-based analysis is required, taking account of the distribution of the force along the tool–workpiece contact. In addition, more detailed studies of interactions such as those between plastic deformation and cleavage fractures of different crystal planes should be conducted. A regression method using machine learning could be used. A more accurate prediction model and other meaningful interaction relationships, which have not been found in this study, are expected to be established. Furthermore, it will be necessary to validate the experimental foundation for the slip/fracture activation model using transmission electron microscopy and focused ion beam techniques.

## ACKNOWLEDGMENTS

This material is based upon work supported by the National Science Foundation under Grant No. CMMI-1844821. The authors gratefully acknowledge kind support from the FANUC Co., Japan for the donation of the ROBONANO α-0iB and A.L.M.T. Co., Japan for the discounted PCD tools. The authors also gratefully acknowledge the use of facilities and instrumentation supported by the NSF through the University of Wisconsin Materials Research Science Center (Grant No. DMR-1720415).

## AUTHOR DECLARATIONS

### Conflict of Interest

The authors have no conflicts to disclose.

## DATA AVAILABILITY

The data that support the findings of this study are available from the corresponding author upon reasonable request.

## REFERENCES

[1]Salem JA, Quinn GD. Fractographic analysis of large single crystal sapphire refractive secondary concentrators. J Eur Ceram Soc 2014;34(14):3271–3281. https://doi.org/10.1016/j.jeurceramsoc.2014.01.029.

[2]Khattak CP, Shetty R, Schwerdtfeger CR, Ullal S. World's largest sapphire for many applications. J Cryst Growth 2016;452:44–48. https://doi.org/10.1016/j.jcrysgro.2015.11.026.

[3]Bifano TG, Dow TA, Scattergood RO. Ductile-regime grinding: A new technology for machining brittle materials. J Eng Ind 1991;113, 184. https://doi.org/10.1115/1.2899676.

[4]Nowak R, Sakai M. The anisotropy of surface deformation of sapphire: Continuous indentation of triangular indenter. Acta Metall Mater 1994;42(8):2879–2891. https://doi.org/10.1016/0956-7151(94)90229-1.

[5]Wang K, Jiang F, Yan L, et al. Study on mechanism of crack propagation of sapphire single crystals of four different orientations under impact load and static load. Ceram Int 2019;45(6):7359–7375. https://doi.org/10.1016/j.ceramint.2019.01.021.

[6]Mizumoto Y, Maas P, Kakinuma Y, Min S. Investigation of the cutting mechanisms and the anisotropic ductility of monocrystalline sapphire. CIRP Ann 2017;66(1):89–92. https://doi.org/10.1016/j.cirp.2017.04.018.

[7]Kwon SB, Min S. Characteristics of force generation on C-, R-, A-and M-planes of single-crystal sapphire during ultra-precision machining. Manuf Lett 2022;33(S):349–354. https://par.nsf.gov/servlets/purl/10391440 (Accessed 2/2.2024).

[8]Yoon HS, Kwon SB, Nagaraj A, Lee S, Min S. Study of stress intensity factor on the anisotropic machining behavior of single crystal sapphire. CIRP Ann 2018;67(1):125–128. https://doi.org/10.1016/j.cirp.2018.04.114.

[9]Kim WK, Xi D, Kim BH. Nanoscale indentation and scratching tests of single crystal sapphire using molecular dynamics simulation. Comput Mater Sci 2019;170:109195. https://doi.org/10.1016/j.commatsci.2019.109195.

[10]Lin J, Jiang F, Wen Q, et al. Deformation anisotropy of nano-scratching on C-plane of sapphire: A molecular dynamics study and experiment. Appl Surf Sci 2021;546:149091. https://doi.org/10.1016/j.apsusc.2021.149091.

[11]Mizumoto Y, Kakinuma Y. Revisit of the anisotropic deformation behavior of single-crystal $CaF_2$ in orthogonal cutting. Precis Eng 2018;53:9–16. https://doi.org/10.1016/j.precisioneng.2018.01.011.

[12]Wang H, Riemer O, Rickens K, Brinksmeier E. On the mechanism of asymmetric ductile–brittle transition in microcutting of (111) $CaF_2$ single crystals. Scr Mater 2016;114:21–26. https://doi.org/10.1016/j.scriptamat.2015.11.030.

[13]Lee YJ, Kumar AS, Wang H. Beneficial stress of a coating on ductile-mode cutting of single-crystal brittle material. Int J Mach Tools Manuf 2021;168:103787. https://doi.org/10.1016/j.ijmachtools.2021.103787.

[14]Yoon HS, Lee S, Min S. Investigation of ductile-brittle transition in machining of yttrium-stabilized zirconia (YSZ). Procedia Manuf 2018;26:446–453. https://doi.org/10.1016/j.promfg.2018.07.052.

[15]Kwon SB, Nagaraj A, Yoon HS, Min S. Study of material removal behavior on R-plane of sapphire during ultra-precision machining based on modified slip-fracture model. Nanotechnol Precis Eng 2020;3(3):141–155. https://doi.org/10.1016/j.npe.2020.07.001.

[16]Clayton JD. A continuum description of nonlinear elasticity, slip and twinning, with application to sapphire. Proc R Soc A 2009;465(2101):307–334. https://doi.org/10.1098/rspa.2008.0281.

[17]Iwasa M, Bradt RC. Fracture toughness of single-crystal alumina. Adv Ceram 1984;10:767.

**Suk Bum Kwon** is presently a Postdoctoral Research Associate in the Department of Mechanical Engineering at the University of Wisconsin–Madison. He earned his Ph.D. from UW–Madison in 2022. His research includes modeling material removal behavior and investigating the mechanisms behind crack formation during ultra-precision machining of single-crystal ceramics.

**Sangkee Min** is currently an Associate Professor in the Department of Mechanical Engineering, University of Wisconsin–Madison. He received his Ph.D. in Mechanical Engineering from U.C. Berkeley in 2001. He has been working on machining processes, burr formation, smart manufacturing, and manufacturing for design (MFD).